

# Characterization of a CMOS pixel sensor for charged particle tracking

---

L. Li,<sup>a</sup> L. Zhang,<sup>a,1</sup> J. N. Dong,<sup>a</sup> J. Liu,<sup>b</sup> and M. Wang<sup>a,1</sup>

<sup>a</sup>*Institute of Frontier and Interdisciplinary Science and Key Laboratory of Particle Physics and Particle Irradiation of Ministry of Education, Shandong University, Qingdao 266237, China*

<sup>b</sup>*Department of Physics, University of Liverpool, Liverpool, L693BX, United Kingdom*

E-mail: [mwang@sdu.edu.cn](mailto:mwang@sdu.edu.cn), [zhang.l@sdu.edu.cn](mailto:zhang.l@sdu.edu.cn)

**ABSTRACT:** A prototype of the CMOS pixel sensor named SUPIX-1 has been fabricated and tested in order to investigate the feasibility of a pixelated tracker for a proposed Higgs factory, namely, the Circular Electron-Positron Collider (CEPC). The sensor, taped out with a 180 nm CMOS Image Sensor (CIS) process, consists of nine different pixel arrays varying in pixel pitches, diode sizes and geometries in order to study the particle detection performance of enlarged pixels. The test was carried out with a <sup>55</sup>Fe radioactive source. Two soft X-ray peaks observed were used to calibrate the charge to voltage factor of the sensor. The pixel-wise equivalent noise charge, charge collection efficiency and signal-to-noise ratio were evaluated. A reconstruction method for clustering pixels of a signal has been developed and the cluster-wise performance was studied as well. The test results show that pixels with the area as large as of  $21\ \mu\text{m} \times 84\ \mu\text{m}$  have satisfactory noise level and charge collection performance, meeting general requirements for a pixel sensor. This contribution demonstrates that the CMOS pixel sensor with enlarged pitches, using the CIS technology, can be used in tracking for upcoming collider detectors akin to the CEPC.

**KEYWORDS:** CMOS pixel sensor, MAPS, charged particle tracking, CEPC, pixelated silicon tracker

ARXIV EPRINT: [2111.00290](https://arxiv.org/abs/2111.00290)

---

<sup>1</sup>Corresponding author.

---

## Contents

<b>1</b>	<b>Introduction</b>	<b>1</b>
<b>2</b>	<b>The test system for SUPIX-1</b>	<b>3</b>
<b>3</b>	<b>The chip test with <math>^{55}\text{Fe}</math></b>	<b>6</b>
3.1	The sensor gain calibration	6
3.2	The anomalous pixel output and a correction method	8
3.3	Reconstruction of the pixel cluster	9
<b>4</b>	<b>Test results</b>	<b>10</b>
<b>5</b>	<b>Conclusions</b>	<b>11</b>

---

## 1 Introduction

The discovery of the Higgs boson [1, 2] opens a new window for studying the fundamental physics principles of the Standard Model (SM) and exploring beyond the SM. The Circular Electron-Positron Collider (CEPC) [3] is a proposed Higgs factory to conduct precision measurements of the Higgs boson. In the conceptual design of the CEPC detector [4], the tracking system involves a silicon tracker, with silicon microstrip sensors as the basic technology. However, a fully pixelated silicon tracker with large pixels is also under consideration and the CMOS Pixel Sensor (CPS) has gained particular interest due to high granularity and low material budget. The CEPC high precision tracking requires a general condition of the single point resolution,  $\sigma_{\text{sp}} < 7\ \mu\text{m}$ , on the transverse plane with regard to the magnetic field. In the longitudinal direction, however, the resolution is undefined, but a loose requirement at least a few times larger than  $7\ \mu\text{m}$  is anticipated. Without considering the effect of charge sharing, the nominal pixel size will be about  $20\ \mu\text{m} \times 80\ \mu\text{m}$  or larger. With the standard CMOS Image Sensor (CIS) process, the CPS pixels realized so far used in high-energy physics experiments are relatively small. For instance, a CPS based vertex detector for the STAR experiment at the Relativistic Heavy Ion Collider (RHIC), Brookhaven National Laboratory, employs pixels of  $20.7\ \mu\text{m} \times 20.7\ \mu\text{m}$  [5]. ALPIDE, another CPS chip which is going to be used for the major upgrade of the inner tracking system for the ALICE experiment at Large Hadron Collider (LHC), CERN, is developed in  $27\ \mu\text{m} \times 29\ \mu\text{m}$  pixels [6].

In order to investigate the feasibility of relatively large pixels based on the standard CMOS imaging process, a prototype chip, named SUPIX-1 (Shandong University PIXEL), has been fabricated and tested. The chip is designed with three different pixel sizes, up to  $21\ \mu\text{m} \times 84\ \mu\text{m}$ , and variant diode geometries. The main purpose of the design is to explore the interplay of the pixel pitch and the diode geometry on the charge collection efficiency. Details of the chip design can be found in ref. [7], while some characteristics are briefed here. As shown in Figure 1(a), the chip contains

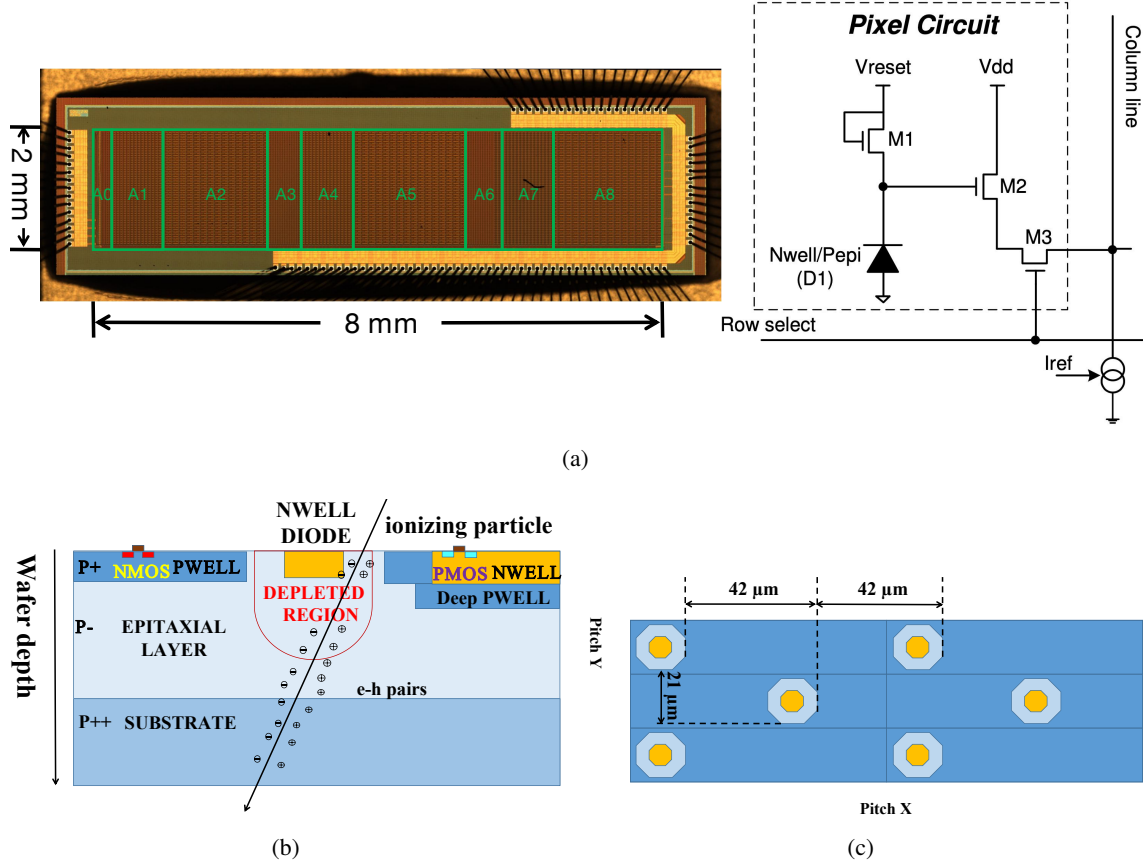


**Figure 1:** Design of the SUPIX-1 sensor: (a) a photograph and the schematic of in-pixel circuit, (b) illustration of a CMOS pixel cross section and (c) the staggered arrangement of diodes in sectors with the largest x-pitch.

nine sectors (only sectors A0, A2, A5, A7 and A8 were accessible during the test) and has an overall area of 2 mm × 8 mm. Each sector contains 64 rows and 16 columns (labelled from C0 to C15) of pixels. The sensitive areas and the pixel pitches of relevant sectors are listed in Table 1. The schematic of in-pixel circuit is also shown in Figure 1(a), employing a 3T architecture. The collected charge in a pixel is converted into the signal voltage through an N-well/P-epitaxial layer diode (D1), as illustrated in Figure 1(b). Combinations of various diode geometries and pixel pitches are implemented in different sectors, as listed in Table 1. The diode surface is defined as the area of the N-well and the diode footprint is the total area formed by the surrounding P-well. A staggered pixel design is implemented in sectors with the largest x-pitch (84 μm), as shown in Figure 1(c), to enhance charge collection. The analog signal of each sector is read out in a rolling shutter mode. The readout time for a frame is 32 μs with a basic clock of 2 MHz.

In this article, we present the test of SUPIX-1 with a radioactive source of  $^{55}\text{Fe}$ . The procedure for characterizing the sensor performance, taking the sector of A0 as an example, is described. The manuscript is organized as follows: a brief introduction of the test system is given in Section 2, steps of the test are elaborated in Section 3, test results are discussed in Section 4, and we conclude in Section 5.

## 2 The test system for SUPIX-1

As shown in Figure 2, the test system for SUPIX-1 consists of readout electronics and a data acquisition system (SupixDAQ). The readout electronics involves a device under test (DUT) board, an analog-to-digital conversion (ADC) board, a field programmable gate array (FPGA) board as well as a personal computer (PC).

**The DUT board** connects to the SUPIX-1 chip by wire bonding and drives analog signal out of the chip.

**The ADC board** digitizes the analog signal with 16-bit ADCs (LTC2323-16) and transmits digitized data to the FPGA board through a FPGA mezzanine card (FMC).

**The FPGA board** configures the ADC board and the DUT board and transmits the digitized data to the PC for data taking through a PCI-express interface. The FPGA is Xilinx Kintex-7 FPGA KC-705.

**The PC** manages data acquisition and records the data.

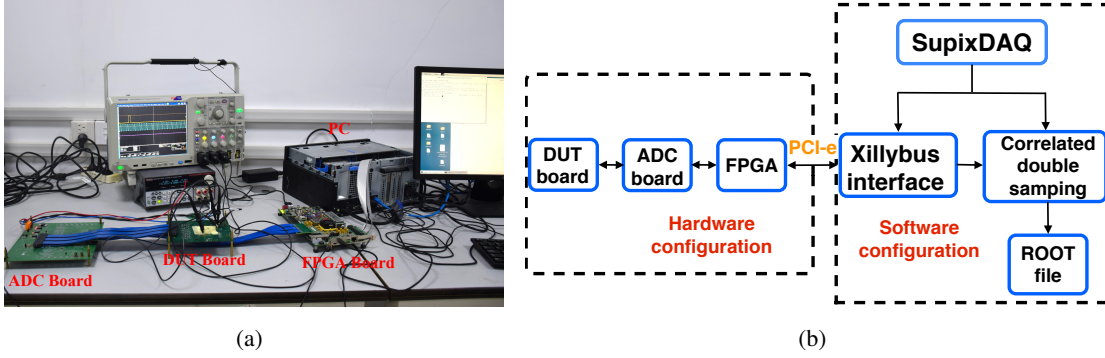


**Figure 2:** (a) Test system for the SUPIX-1 sensor and (b) working flow of the system.

The readout electronics was calibrated with the input voltage from a signal generator (Tektronix AFG3252C). As shown in Figure 3, the linearity is good in the range of the input voltage. The electronics calibration constant is defined as

$$A \equiv \frac{\text{ADC}}{\text{Voltage}}, \quad (2.1)$$

where ADC represents the ADC count. The calibration resulted in  $A = (7.76 \pm 0.04) \text{ ADC/mV}$ .

As the readout of SUPIX-1 is in rolling shutter, the SupixDAQ takes data in frames continuously and implements the correlated double sampling (CDS) method. As demonstrated in Figure 4, the ADC distribution of a frame is subtracted by that of a preceding frame, resulting in the CDS distribution. The CDS can cancel the pixel-wise fluctuation of baseline and suppress the fixed pattern noise significantly. Hence, the CDS value of ADC, also called ADC, will be used in the work unless explicitly distinguished.

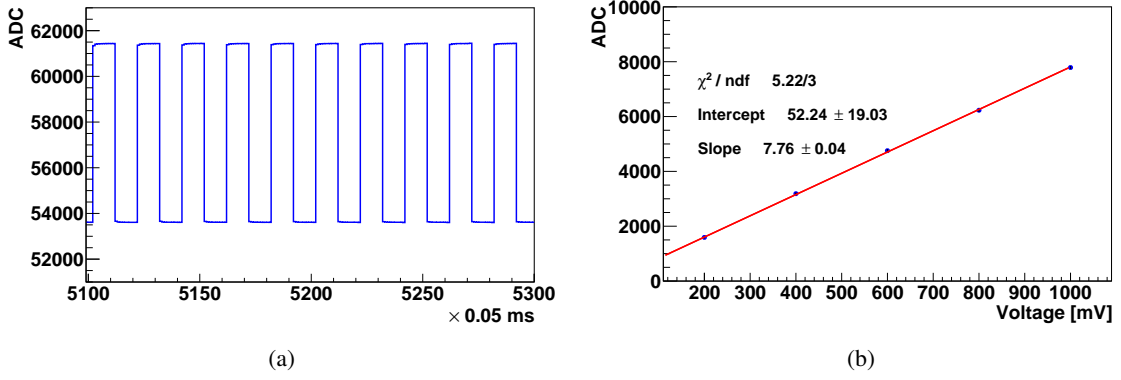


**Figure 3:** Calibration for the readout electronics: (a) the ADC output of an input square wave with 1 V amplitude and 1 kHz frequency and (b) the ADC output as a function of the input voltage together with a linear function fit.

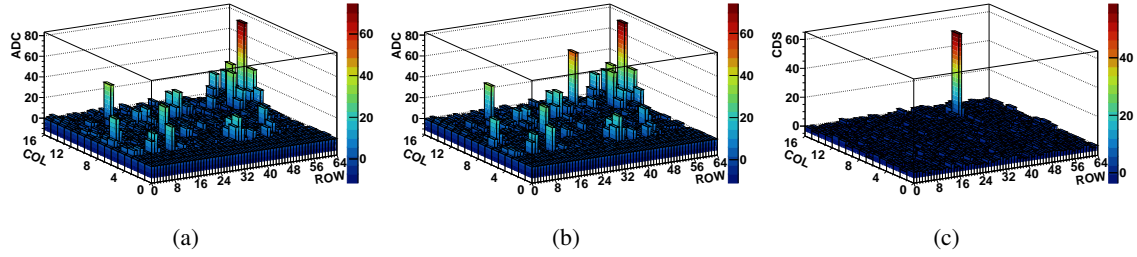


**Figure 4:** Demonstration of the correlated double sampling (CDS) method: (a) the ADC output of a frame, (b) the ADC output of a preceding frame and (c) the result of (a) minus (b), namely CDS of the frame.

In order to calibrate noise pixel-by-pixel, a *noise run* is taken before taking data with a radioactive source, namely a *calibration run*. As an example, the noise level before and after CDS of each pixel in the sector of A0 is shown in Figure 5(a). Both distributions of the mean and the standard deviation of the pixel-by-pixel noise are shown in Figure 5(b) and (c), separately. Values of the latter are noise calibration constants. During the test, because the pixels of a few columns (C0, C1, C4 and C7) did not work properly and the reconstruction of the pixel cluster would be studied, only the pixels of columns from C8 to C15 were used.

The noise calibration constants are used in the calibration run to define the hit pixel, with the condition of  $-CDS > 8\sigma$ . A frame having at least one hit is triggered for recording for off-line analysis. The *trigger threshold* of  $8\sigma$  is chosen to suppress the noise hit as many as possible while losing the physical hit as few as possible. Figure 6(a) shows the fake-trigger rate and the fake-hit rate as functions of the trigger threshold for a noise run. For the threshold beyond  $5\sigma$ , the fake-trigger rate approaches zero and the fake-hit rate decreases exponentially as the trigger threshold increases. Figure 6(b) shows, for a calibration run, the distribution of the signal-to-noise ratio (SNR) of the seed pixel, which has the largest value in a frame, and the SNR is just  $-CDS/\sigma$ . Obviously the cut

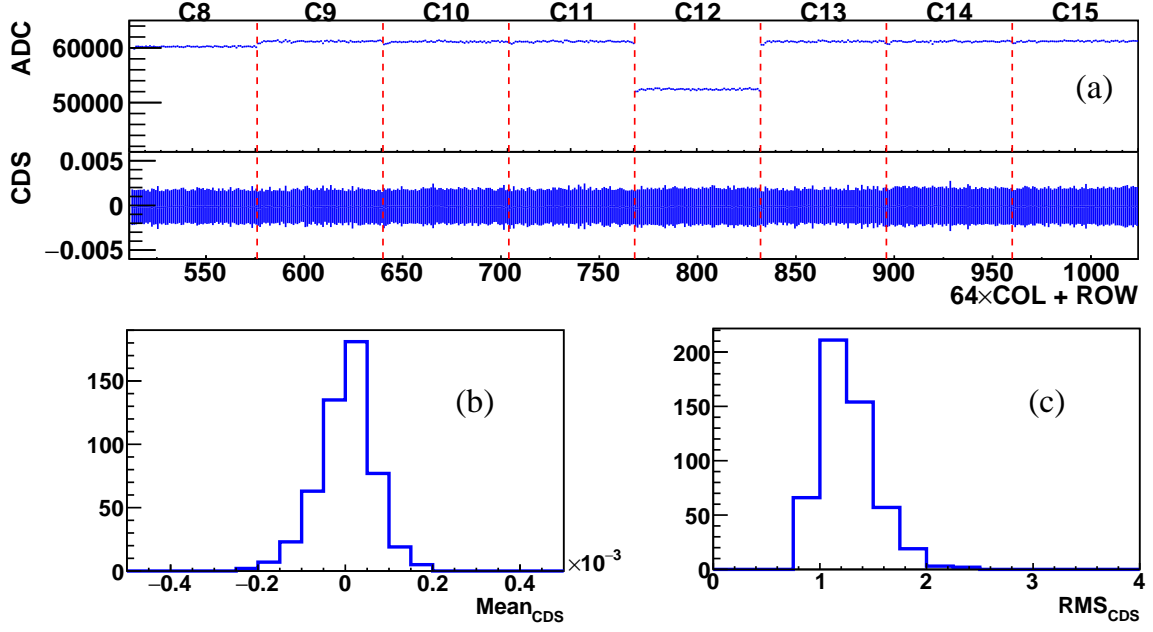


**Figure 5:** Results of a noise run for the sector of A0: (a) profiles of the mean and standard deviation of the pixel-by-pixel distribution of the raw ADC (up) and the ADC after CDS (down), and distributions of the CDS mean (b) and standard deviation (c) of pixels. Only pixels of the columns from C8 to C15 are shown.

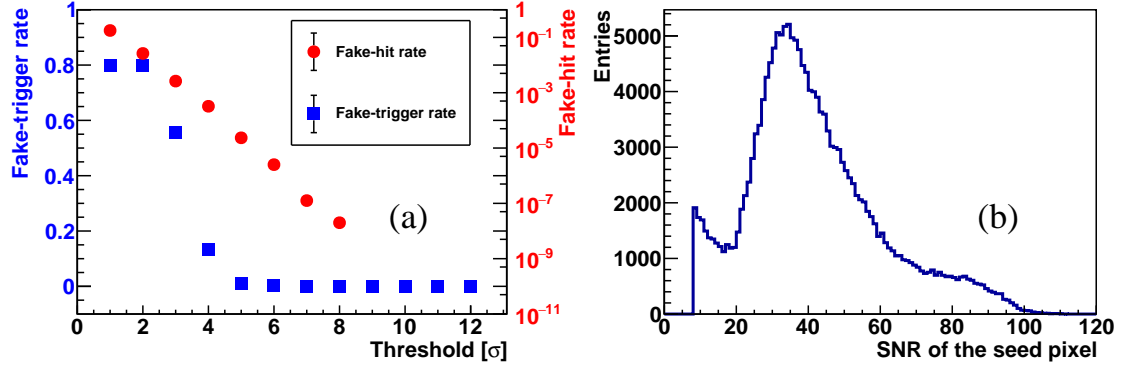


**Figure 6:** (a) The fake-trigger rate (left axis) and the fake-hit rate (right axis) versus the trigger threshold, and (b) the SNR distribution of the seed pixel. See the text for explanations.

on  $8\sigma$  loses physical hits rarely, if any. In addition, the SNR distribution of all pixels for the same run is shown in Figure 10(a). With the chosen threshold, the rates of fake trigger and fake hit are  $(7 \pm 3) \times 10^{-6} \text{ trigger}^{-1}$  and  $(1.8 \pm 0.6) \times 10^{-8} \text{ pixel}^{-1} \text{ trigger}^{-1}$ , respectively.

A hit map of the pixel for a sector is shown in Figure 7(a). There are much more hits in the first two rows than in the others, which happens in all sectors. The cause is unknown yet, and the two rows of pixels were excluded from searching the seed pixel. Corresponding distributions of the number of hit pixels per frame and the CDS of hit pixels are shown in Figure 7(b) and Figure 7(c), respectively. As the CDS value of the hit pixel is negative, we use its opposite value in the following

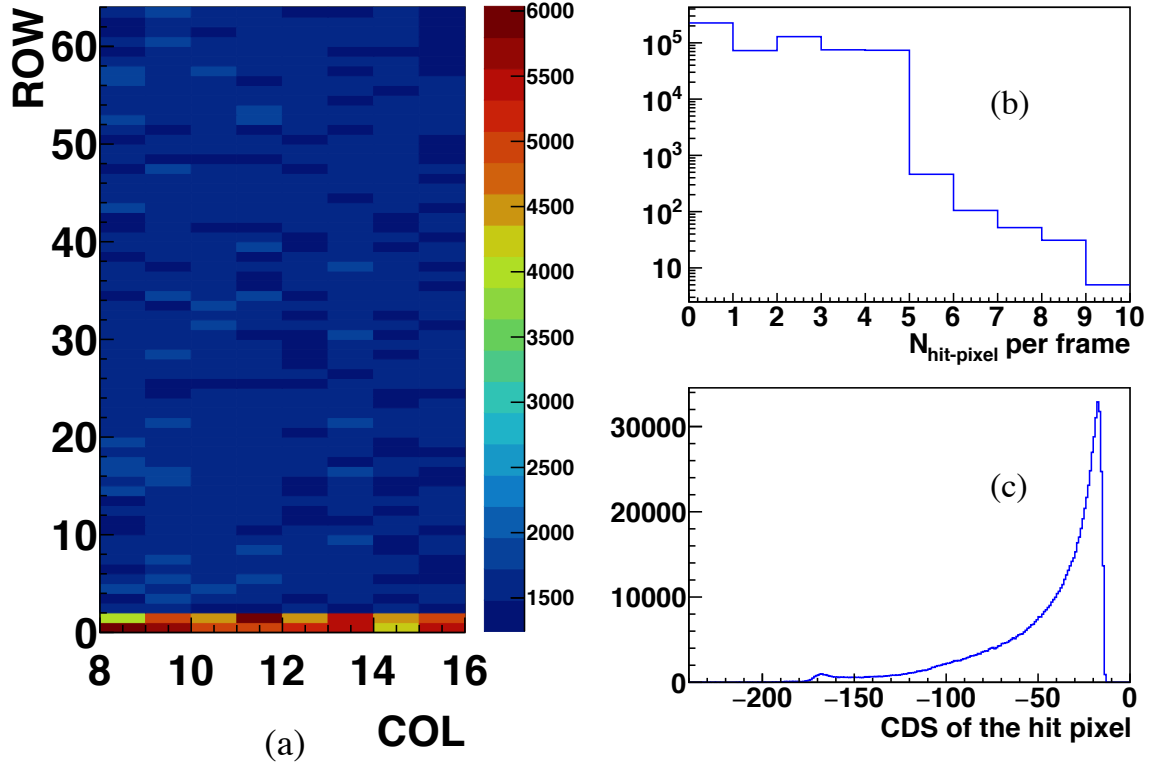


**Figure 7:** Sensor performance under  $^{55}\text{Fe}$  irradiation: (a) hit map of pixels, (b) distribution of the number of hit pixels per frame and (c) distribution of the ADC after CDS of the hit pixel.

text for convenience.

### 3 The chip test with $^{55}\text{Fe}$

#### 3.1 The sensor gain calibration

The sensor gain calibration is carried out using the soft X-rays of  $^{55}\text{Fe}$ , of which  $k\text{-}\alpha$  (5.9 keV) accounts for 24.4% and  $k\text{-}\beta$  (6.5 keV) for 2.9% in yield. A 5.9 keV photon can generate about 1640 electron-hole pairs when absorbed in silicon bulk, assuming a constant value, 3.6 eV at room temperature, is required to create an electron-hole pair [8]. In most cases, the ionized electrons are collected by several pixels, forming a pixel cluster, through thermal diffusion in the epitaxial layer. Specifically, the electrons will be collected by a single pixel if the photons are absorbed in the depleted region of that pixel, forming the full energy peak [9]. Figure 8 shows, for instance, a distribution of the seed-pixel ADC, on which two full-energy peaks (*calibration peaks*) around 169 and 185 can be observed, corresponding to the X-rays of  $k\text{-}\alpha$  and  $k\text{-}\beta$ , respectively.

As shown in Figure 8, the full spectrum can be fitted well with a combination of component functions. The addition of a crystal ball function (CB, blue dashed line) for  $k\text{-}\alpha$  peak and a Gaussian function ( $G_\beta$ ) for  $k\text{-}\beta$  peak is used to describe the calibration peaks. The power-law tail of the crystal ball function is justified considering the partial energy deposition in the depleted region. The peak with the highest amplitude, named the *collection peak*, is described by two Gaussian functions ( $G1$

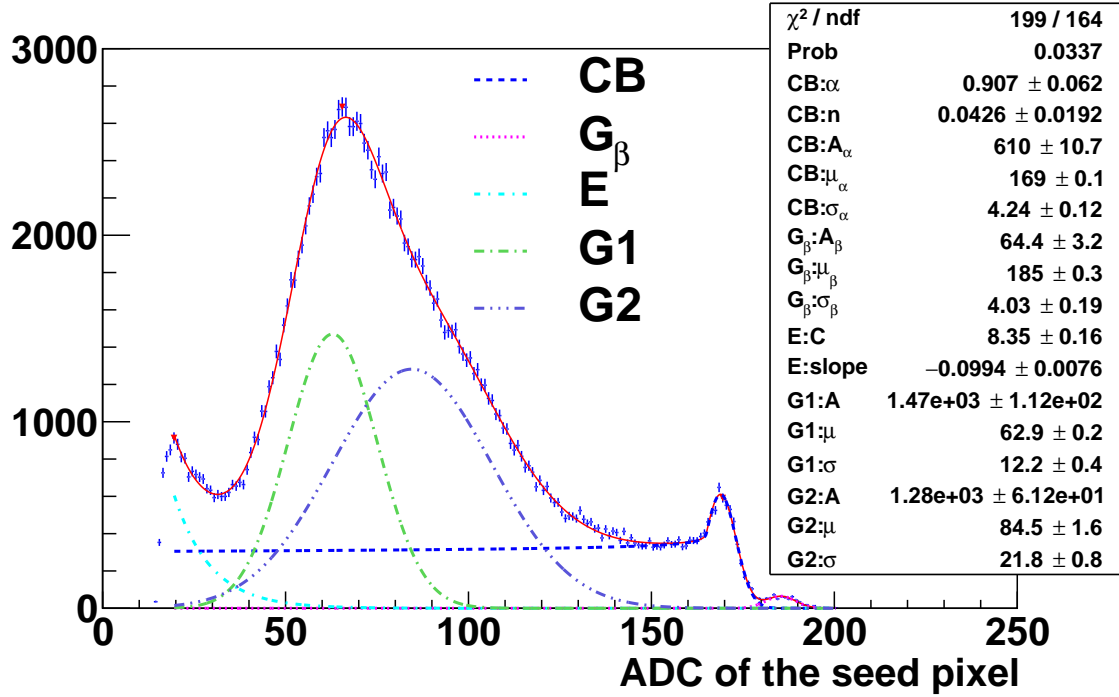


**Figure 8:** The distribution of the seed-pixel ADC, irradiated with  $^{55}\text{Fe}$ , together with a full spectrum fit. See the text for explanations.

and G2) superposed on the crystal-ball tail. There are two ways that ionized electrons can contribute to the collection peak: (a) directly by an incident X-ray photon in the vicinity of the seed pixel, and (b) by charge sharing from neighbor pixels. Hence, the use of two Gaussians could be justified. The Landau distribution fails to describe the collection peak because most incident X-ray photons are fully absorbed in the epitaxial layer. Towards the low end of the spectrum, an exponential function (E) is added to describe the pedestal associated with the electronic noise.

The pixel gain is defined as

$$G = \frac{\text{ADC}_{\text{peak}} - \text{ADC}_{\text{pedestal}}}{Q}, \quad (3.1)$$

where  $Q$  is for charge. Assuming the linear response, the gain can be obtained by comparing the locations of the two calibration peaks, with no need for pedestal subtraction. After the gain calibration, the charge-to-voltage factor (CVF) can be determined by

$$\text{CVF} = \frac{G}{A}, \quad (3.2)$$

where  $A$  is the electronics calibration factor in eq. (2.1). Also, the fixed pattern noise shown in Figure 5(c) can be transformed into the equivalent noise charge (ENC),

$$\text{ENC} = \frac{\langle \text{RMS}_{\text{noise}} \rangle}{G}, \quad (3.3)$$

where  $\langle \text{RMS}_{\text{noise}} \rangle$  is the mean of  $\text{RMS}_{\text{CDS}}$  in Figure 5(c). The ENC and the CVF are inversely correlated.



We use the fitted location of the collection peak, namely the most probable value (MPV) of ADC, to characterize the charge collection efficiency (CCE) and the SNR of the pixel for a sector,

$$\text{CCE}_{\text{pixel}} = \frac{\text{ADC}_{\text{MPV, seed}}}{\text{ADC}_{k-\alpha, \text{seed}}}, \quad (3.4)$$

$$\text{SNR}_{\text{pixel}} = \frac{\text{ADC}_{\text{MPV, seed}}}{\langle \text{RMS}_{\text{noise}} \rangle}, \quad (3.5)$$

where  $\text{ADC}_{k-\alpha, \text{seed}}$  is the location of the  $k-\alpha$  peak. Results for all sectors are summarized in Table 1.

### 3.2 The anomalous pixel output and a correction method

An anomaly was observed when we studied reconstruction for the pixel cluster. For each frame in a  $5 \times 5$  array centering at the seed pixel, we figured out the top five pixels, including the seed pixel, based on the ordering of ADC. Figure 9(a) shows the relative position distribution of the top five pixels. Among four adjacent pixels, the frequency of the pixel in the same column as the seed but being read out immediately after the seed, tagged as PIX\_F, is anomalously high. In Figure 9(b), the ADC of each adjacent pixel is drawn as a function of the seed-pixel ADC, and the anomaly is significant. Particularly, in the ADC region greater than 170, where the seed pixel absorbs mostly all ionized charges, the ADC of the three normal pixels fluctuates around zero. In comparison, the ADC of the anomalous pixel increases linearly as the seed ADC increases. The anomaly might be related to the rolling shutter readout, but remains unknown yet.

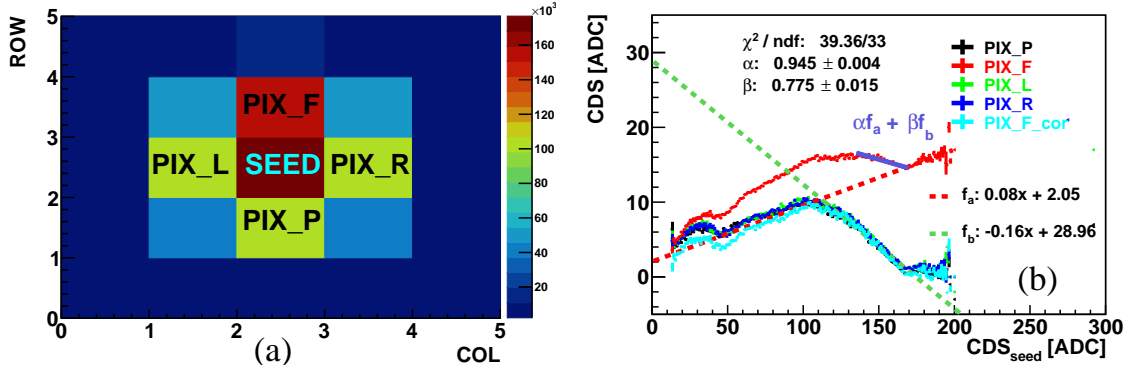


**Figure 9:** (a) Distribution of the relative position of the top five pixels ordered in ADC within a  $5 \times 5$  array centering at the seed pixel per frame, and (b) the ADC of each adjacent pixel and the corrected ADC of the anomalous pixel as a function of the seed-pixel ADC. The tag PIX\_F stands for the anomalous pixel. See the text for explanations.

An empirical method was developed to correct the output of the anomalous pixel, that is also illustrated in Figure 9(b). A linear function,  $f_a(x)$ , where  $x$  stands for ADC of the seed pixel, is obtained via fitting the anomalous curve in the range of  $x > 170$ . Another linear function,  $f_b(x)$ , is obtained via fitting the normal curves in the range of  $130 < x < 170$ . Then a linear combination of the two functions,  $\alpha f_a + \beta f_b$ , is fitted against the anomalous curve in the same fit range as that of  $f_b$  to determine the coefficients  $\alpha$  and  $\beta$ . Finally, the anomaly is corrected with the equation

$$\text{PIX\_F\_cor} = \frac{\text{PIX\_F}(x) - \alpha f_a(x)}{\beta}, \quad (3.6)$$

where  $\text{PIX\_F}$  and  $\text{PIX\_F\_cor}$  are the original and corrected ADCs of the anomalous pixel, respectively. As shown in Figure 9(b), the correction (cyan curve) is reasonable, but it is somehow underestimated in the range of  $\text{CDS}_{\text{seed}} < 100$  ADC. The effect of the bias to the pixel clustering is negligible based on further study.

### 3.3 Reconstruction of the pixel cluster

Most X-ray photons of  $^{55}\text{Fe}$  deposit their energy in the epitaxial layer and the ionized electrons are collected by a cluster of pixels. Hence, the clustering algorithm as well as the property of the cluster was studied. We tried several methods to reconstruct the cluster of pixels. Their performance was similar and one of them is reported here.

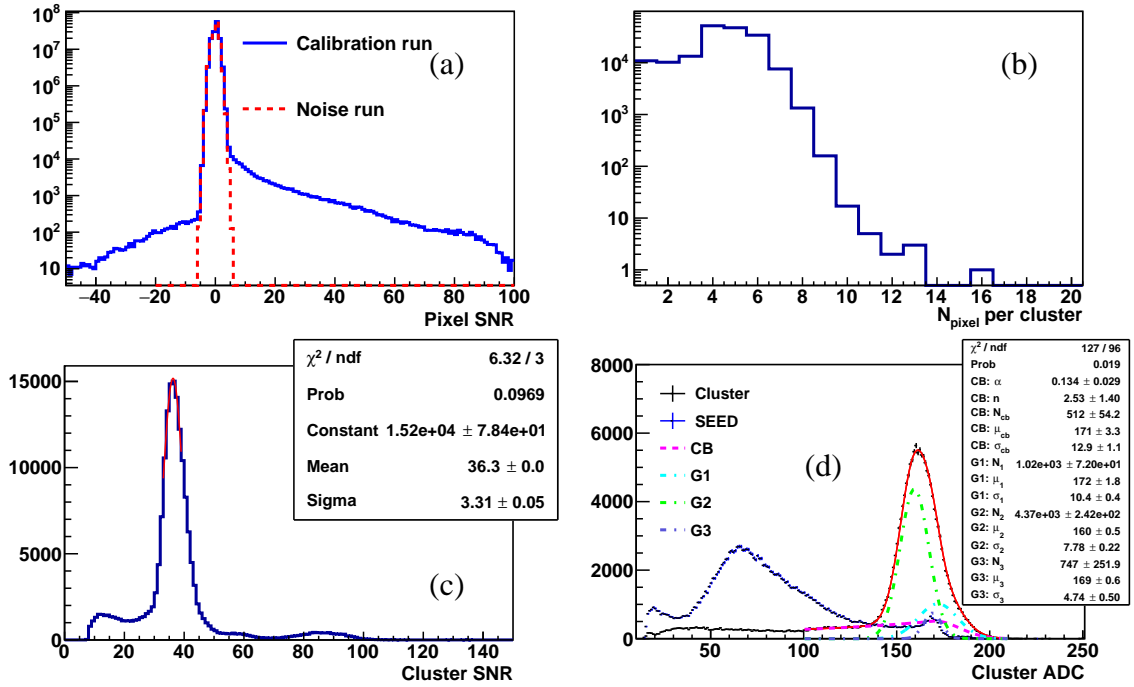


**Figure 10:** Reconstruction for the cluster of pixel: (a) distributions of the pixel SNR for a noise run and a calibration run, (b) distribution of the number of pixels per cluster, (c) distribution of the cluster SNR, and (d) distribution of the cluster ADC and a fit for the distribution, together with the distribution of the seed-pixel ADC for comparison. See the text for explanations.

A cluster is defined by a group of adjacent fired pixels, which have signals above a *clustering threshold*. The cluster reconstruction starts with a seed pixel, selects neighboring fired pixels including diagonal ones, and repeats the selection for newly selected pixels until there are no fired neighbors anymore or reaching an edge of the pixel array. The clustering threshold for the fired pixel is based on the SNR of individual pixels. As indicated in Figure 10(a), the threshold is set to 3.1, corresponding to less than one per mil of noise pixels leaked into clustering pixels. The number of pixels and the SNR of the reconstructed cluster are shown in Figure 10(b) and (c), respectively.

The cluster SNR is evaluated as

$$\text{SNR}_{\text{cluster}} = \frac{\sum_i \text{ADC}_i}{\sqrt{\sum_i \sigma_i^2}}, \quad (3.7)$$

where  $\text{ADC}_i$  and  $\sigma_i$  are the ADC and the noise of the  $i$ -th pixel. The numerator is just the ADC of a cluster. Most of the clusters consist of 4 or 5 pixels and have the SNR greater than 25. On the SNR distribution, there is a small peak at about 85, which attributes mainly to the single-pixel clusters.

The distribution of the cluster ADC is shown in Figure 10(d), together with that of the seed pixel for comparison. The distribution can be fitted well with a few Gaussian functions superposed with a crystal ball function. The peak of the distribution shifts toward the left with regard to the  $k\text{-}\alpha$  peak. The shift, indeed, depends on the clustering threshold, which is a compromise between the noise pixel and the physically fired pixel. We can use the location of the peak to define the charge collection efficiency of the cluster,

$$\text{CCE}_{\text{cluster}} = \frac{\text{ADC}_{\text{MPV, cluster}}}{\text{ADC}_{k\text{-}\alpha, \text{seed}}}. \quad (3.8)$$

Both of the  $\text{SNR}_{\text{cluster}}$  and  $\text{CCE}_{\text{cluster}}$  can characterize the performance of the sensor under test. Results are summarized in Table 1, where the MPV of  $\text{SNR}_{\text{cluster}}$ , as shown in Figure 10(c), is reported.

## 4 Test results

All available sectors have been tested with the previously described procedure. Test results as well as geometrical parameters of the sensor are listed in Table 1, where the pixel-wise quantities are defined in Section 3.1 and the cluster-wise quantities are defined in Section 3.3.

For all sectors, the CVFs and the ENC of the pixels are consistent within uncertainties. The means of pixel-by-pixel ENC distributions in each sector are all below  $14\text{ e}^-$ , and have the RMS spreads of about 40%. Taking A0 as a reference, variations of the means among sectors are within 10%, less than the uncertainties.

As for the pixel-wise performance of charge collection, the SNRs are consistent within uncertainties, whereas the CCEs, and the means of SNRs exhibit geometry dependence similarly. The sectors of A2 and A0 have almost the same geometry configuration except that the x-pitch of A2 is four times that of A0. The CCE of A2 decreases about 19% of that of A0, while the mean of SNR decreases about 6% only. The sectors of A2, A5 and A8, consisting of the largest pixels, have the same pixel pitches and different areas of the diode surface and footprint. Among them, the CCE and SNR of A8 are the best, very close to those of A0, whereas those of A5 are the worst. It implies that not only the absolute size of the diode surface but also the surface to footprint ratio influences the performance. The sectors of A7 and A8 have similar diode dimensions, but the x-pitch of A7 is half of A8's. In addition, the diodes of A8 have a staggered arrangement, therefore the diode distribution density is half of that of A7 evenly. That explains why A7, due to charge sharing, has smaller CCE than A8 does. The observations confirm our previous simulation for the sensor design, as shown in Figure 3 and 4 in ref. [7].

For the cluster-wise performance, all sectors perform well, having CCEs and SNRs greater than 90% and 30, respectively. Again the SNRs are consistent within uncertainties, and their means

depend weakly on geometrical configuration. On the other hand, the CCEs are almost geometry independent, within about 5% variation referring to the CCE of A0, and A7 performs the best.

**Table 1:** Geometrical parameters of the SUPIX-1 sensor and test results with a  $^{55}\text{Fe}$  radioactive source. CVF is for the charge-to-voltage factor, ENC is for the equivalent noise charge, CCE is for the charge collection efficiency and SNR is for the signal-to-noise ratio. The uncertainties of the CCEs are on the most probable values, while the uncertainties of the others are of the distribution. See the text for more explanations.

Sector		A0	A2	A5	A7	A8
Sensitive Area x (mm)		0.3	1.3	1.3	0.7	1.3
Sensitive Area y (mm)		1.3				
Pixel Pitch x ( $\mu\text{m}$ )		21	84	84	42	84
Pixel Pitch y ( $\mu\text{m}$ )		21				
Diode Surface ( $\mu\text{m}^2$ )		8	8	12	20	20
Diode Footprint ( $\mu\text{m}^2$ )		11	11	18	44	50
Pixel	CVF ( $\mu\text{V}/\text{e}$ )	13 $\pm$ 5	14 $\pm$ 5	12 $\pm$ 4	14 $\pm$ 4	13 $\pm$ 5
	ENC (e)	13 $\pm$ 5	12 $\pm$ 5	13 $\pm$ 5	12 $\pm$ 4	12 $\pm$ 5
	CCE (%)	39.1 $\pm$ 1.0	31.7 $\pm$ 0.7	27.5 $\pm$ 0.6	30.4 $\pm$ 0.8	37.2 $\pm$ 0.7
	SNR	52 $\pm$ 11	49 $\pm$ 10	36 $\pm$ 8	42 $\pm$ 9	53 $\pm$ 11
Cluster	CCE (%)	95.6 $\pm$ 0.5	90.3 $\pm$ 0.4	93.8 $\pm$ 0.5	96.8 $\pm$ 0.4	92.4 $\pm$ 0.6
	SNR	36 $\pm$ 3	33 $\pm$ 2	32 $\pm$ 2	36 $\pm$ 3	36 $\pm$ 3

## 5 Conclusions

Using a radioactive source of  $^{55}\text{Fe}$ , we have characterized the SUPIX-1 pixel sensor implemented in a 180 nm CMOS imaging process. The sensor, consisting of sectors with different pixel configurations, is aimed to investigate detection performance of the large pixel, meeting requirements of a proposed pixelated silicon tracker at CEPC. The full energy peaks corresponding to the  $k\text{-}\alpha$  and  $k\text{-}\beta$  X-rays of  $^{55}\text{Fe}$  have been observed and are used to calibrate the pixel gain and to obtain the pixel-wise CVF, ENC, CCE and SNR. A preliminary algorithm to reconstruct the signal cluster of pixels has been developed and the cluster-wise CCE and SNR are determined. During the study of reconstruction, an anomaly in the pixel output is observed and an empirical correction method has been developed.

With our chosen threshold for data taking, the fake-hit rate is in the order of  $10^{-8}$  pixel $^{-1}$  trigger $^{-1}$ . The pixels of all available sectors have low noise, with all ENC being about 13 e $^{-}$  and almost the same within the uncertainty of about 5 e $^{-}$ . For different sectors, the pixel-wise CCEs depend on the geometry configuration significantly, whereas the cluster-wise CCEs do not and are greater than 90% for all. The SNRs of both pixel and cluster in all sectors are high, mostly above 30, and are consistent within uncertainties.

Our test results demonstrate that large pixels, like those in the sector of A8, satisfy typical requirements of pixel detectors in the sense of noise and charge collection efficiency. They are

practical for tracking at CEPC, since CVF and ENC do not constrain pixel performance at the large sizes. In addition, the pixel performance of charge collection depends not only on the pitch size but also on the diode design, including the areas of surface and footprint as well as the arrangement of position. It would be potentially possible to explore the design of even larger pixels, optimized towards specific requirements of different detectors.

## Acknowledgments

This work has been supported by the National Natural Science Foundation of China(U1232202, U2032203 and 12075142), the Ministry of Science and Technology of China (2018YFA0404302) and Shandong Provincial Natural Science Foundation (ZR2020MA102).

## References

- [1] ATLAS collaboration, *Observation of a new particle in the search for the Standard Model Higgs boson with the ATLAS detector at the LHC*, *Phys. Lett. B* **716** (2012) 1 [[arXiv:1207.7214](#)].
- [2] CMS collaboration, *Observation of a New Boson at a Mass of 125 GeV with the CMS Experiment at the LHC*, *Phys. Lett. B* **716** (2012) 30 [[arXiv:1207.7235](#)].
- [3] The CEPC Study Group, “CEPC Conceptual Design Report: Volume 1 - Accelerator.” 2018, [arXiv:1809.00285](#).
- [4] The CEPC Study Group, “CEPC Conceptual Design Report: Volume 2 - Physics & Detector.” 2018, [arXiv:1811.10545](#).
- [5] G. Contin et al., *The STAR MAPS-based PiXeL detector*, *Nucl. Instrum. Meth. A* **907** (2018) 60 [[arXiv:1710.02176](#)].
- [6] ALICE collaboration, *The ALPIDE pixel sensor chip for the upgrade of the ALICE Inner Tracking System*, *Nucl. Instrum. Meth. A* **845** (2017) 583.
- [7] L. Zhang, M. Fu, Y. Zhang et al., *Investigation of CMOS pixel sensor with 0.18  $\mu\text{m}$  CMOS technology for high-precision tracking detector*, *JINST* **12** (2017) C01011.
- [8] PARTICLE DATA GROUP collaboration, *Review of Particle Physics*, *PTEP* **2020** (2020) 083C01.
- [9] G. Deptuch et al., *Design and testing of monolithic active pixel sensors for charged particle tracking*, *IEEE Trans. Nucl. Sci.* **49** (2002) 601.